

Bayesian Inference of Neutron Star Properties in $f(Q)$ Gravity Using NICER Observations

Sneha Pradhan^{1,2,*}, N. K. Patra^{1,2,†}, Kai Zhou^{2,‡} and P. K. Sahoo^{1,2,§}

¹*Department of Mathematics, Birla Institute of Technology and Science, Pilani, Hyderabad Campus, Jawahar Nagar, Kapra Mandal, Medchal District, Telangana 500078, India and*

²*School of Science and Engineering, The Chinese University of Hong Kong, Shenzhen (CUHKShenzhen), Guangdong, 518172, China*

(Dated: January 26, 2026)

In this work, we investigate neutron stars (NSs) in the strong field regime within the framework of symmetric teleparallel $f(Q)$ gravity, considering three representative models: linear, logarithmic, and exponential. While Bayesian studies of NS observations are well established in General Relativity and curvature based modified gravity theories, such analyses in $f(Q)$ gravity remain largely unexplored. We perform a Bayesian inference analysis by confronting theoretical NS mass-radius predictions with NICER observations of PSR J0030+0451, PSR J0740+6620, PSR J0437+4715, and PSR J0614+3329. The dense matter equation of state is fixed to DDME2 in order to isolate the effects of modified gravity on NS structure. Our results show that the exponential $f(Q)$ model is statistically preferred over the linear and logarithmic cases, as confirmed by Bayes factor comparisons, and exhibits well-constrained. For this model, we obtain a radius and tidal deformability at $1.4 M_{\odot}$ of $R_{1.4} = 11.27^{+0.53}_{-0.36}$ km and $\Lambda_{1.4} = 156.95^{+84.02}_{-41.73}$, respectively, consistent with current observational constraints. These results highlight the potential of NSs as powerful probes of symmetric teleparallel gravity in the strong field regime.

PACS numbers:

I. INTRODUCTION

Einstein's General Theory of Relativity (GR) [1] provides a remarkably successful theory of gravitation, accurately explaining gravitational phenomena from Solar System tests to cosmological scales. In this framework, gravity is not treated as a fundamental force, but rather emerges from the curvature of spacetime induced by the presence of matter and energy [2]. Despite its empirical success, GR encounters conceptual and observational challenges when applied to the entire Universe [3]. In particular, the appearance of spacetime singularities signals a breakdown of the classical theory, while the phenomena attributed to dark matter and dark energy require the introduction of unknown components within the standard GR framework. These issues strongly motivate the exploration of modified theories of gravity (MG) [4].

In recent years, there has been growing interest in MG as possible explanations for the observed late-time acceleration of the Universe. This accelerated expansion has been firmly established by several

independent observational probes, including Type Ia supernovae, measurements of cosmic microwave background anisotropies, and large-scale structure surveys [5–8]. Although the cosmological constant offers the simplest description consistent with these observations, its interpretation within the framework of quantum field theory remains unsatisfactory. In particular, the observed value of the cosmological constant is much smaller than the theoretical predictions, giving rise to the well-known fine-tuning and coincidence problems [9, 10]. These unresolved issues have motivated a wide range of alternative ideas, including dynamical dark energy scenarios and modifications of gravity itself [11–13].

In the standard Riemannian formulation of GR, gravity is described as a manifestation of the curvature of the spacetime manifold. From an effective field theory perspective, it is natural to expect that higher-order geometric contributions may become relevant at high energy scales or in strong-gravity regimes. This expectation has motivated several extensions of GR, among which two widely studied approaches are the introduction of additional scalar degrees of freedom and the generalization of the Einstein–Hilbert action by replacing the Ricci scalar R with a nonlinear function $f(R)$ [14–17]. Alternatively, GR admits equivalent formulations based on different choices of affine connections, offering distinct geometric interpretations of

*Electronic address: snehapradhan2211@gmail.com

†Electronic address: nareshkumarpatra3@gmail.com

‡Electronic address: zhoukai@cuhk.edu.cn

§Electronic address: pksahoo@hyderabad.bits-pilani.ac.in

gravitation while preserving dynamical equivalence at the level of field equations [18, 19]. One such formulation is the teleparallel equivalent of General Relativity (TEGR), where gravity is encoded in spacetime torsion rather than curvature, the tetrad field serves as the fundamental dynamical variable, and the gravitational action is constructed from the torsion scalar T , with the curvature identically vanishing [19, 20]. A further geometric reformulation is provided by the symmetric teleparallel equivalent of General Relativity (STEGR), in which both curvature and torsion vanish, and gravity is entirely described by the nonmetricity of spacetime through the disformation tensor [21, 22]. In this framework, the gravitational interaction is governed by the nonmetricity scalar Q , which forms the basis for the construction of modified theories such as $f(Q)$ gravity. These theories offer a novel and geometrically distinct extension of GR, with promising applications in cosmology and astrophysics. In this work, we investigate the internal structure of neutron stars (NSs) within the framework of $f(Q)$ gravity by considering three representative functional forms of the theory, namely linear, logarithmic and exponential models [23–25]. These choices encompass both linear and nonlinear extensions of the gravitational action with respect to the nonmetricity scalar Q , leading to modified field equations that govern stellar equilibrium. By systematically analyzing these models, we aim to assess how departures from general relativity (GR) influence the macroscopic properties of NSs, such as their mass–radius relations and internal profiles. MG theories such as the $f(Q)$ models considered here are well motivated, as they can potentially explain gravitational phenomena without invoking additional dark matter. However, any viable theory must satisfy broad astrophysical and observational constraints. Notably, $f(Q)$ models have been extensively studied in cosmology and shown to fit data well, reproducing late-time cosmic acceleration, dynamical dark energy behavior, and stable phase-space evolution [26, 27]. Crucially, a complete theory must also address the strong-field regime. NSs are the compact objects with intense gravitational fields and extreme physics provide a powerful test of $f(Q)$ gravity beyond cosmology.

In parallel with advances in gravitational theory, rapid progress in neutron-star observations has established compact objects as powerful probes of strong-field gravity. The dense matter equation of state (EoS) governs neutron-star properties such as the mass–radius relation, tidal deformability, oscillation modes, and internal structure, which in turn determine observable

signatures in gravitational-wave (GW), electromagnetic, and thermal emissions [28–33]. Over the past decade, precise measurements have significantly constrained the EoS. In particular, the discovery of NSs with masses near $2M_\odot$ has ruled out many overly soft EoS models, imposing stringent limits on matter at supranuclear densities [34–37]. Further constraints have been provided by observations with the NS Interior Composition Explorer (NICER), which has provided the first simultaneous mass–radius measurements of rotation-powered millisecond pulsars through relativistic X-ray pulse-profile modeling. In particular, analyses of PSR J0030+0451 and PSR J0740+6620 favor radii in the range $R \sim 12$ –14km for NSs with masses near $1.4M_\odot$ and $\sim 2M_\odot$, respectively, thereby ruling out both extremely soft and overly stiff EoS [38–41]. Complementary constraints arise from GW observations of binary neutron-star mergers, most notably GW170817, which impose stringent upper bounds on the dimensionless tidal deformability of a canonical $1.4M_\odot$ NS, $\Lambda_{1.4} \lesssim 800$, further narrowing the space of viable EoS models [42].

Within GR, a number of studies have combined multimessenger NS observations to place stringent constraints on stellar structure and dense-matter physics. More recently, similar strategies have been applied to MG, where NS observables such as maximum mass–radius relations and tidal deformabilities, as sensitive probes of deviations from GR and of additional model parameters [43–46]. A considerable number of studies have investigated the dynamical stability of neutron stars within various modified theories of gravity, including $f(R)$ gravity [46–48], Rainbow–Rastall gravity [49], and $f(T)$ gravity [50]. These works have provided valuable theoretical insights into how deviations from general relativity can influence neutron-star stability. However, in most of these analyses, the model parameters are chosen phenomenologically often through trial-and-error procedures, without being systematically constrained by observational data. Consequently, the astrophysical viability of such models remains largely untested against current observations. This motivates the need for a systematic investigation in which modified-gravity neutron-star models are tested against observational constraints, thereby bridging the gap between theoretical consistency and astrophysical viability. In this context, Bayesian inference has emerged as a powerful framework for confronting theoretical models with observational data. Bayesian analyses combining NICER mass–radius measurements with GW constraints from binary NS mergers have yielded statistically robust constraints on the dense-matter EoS

within GR [51–55]. These methods have subsequently been extended to MG, notably $f(R)$ and related theories, enabling the joint inference of the EoS and gravity-sector parameters by maintaining consistency with NICER observations, GW signals, and massive pulsars [56, 57]. Such studies demonstrate that compact-object observations can impose stringent bounds on departures from GR. Despite this progress, most observationally driven constraints have focused on curvature-based extensions of gravity, STEGR has received comparatively little attention from an observational standpoint. In particular, although $f(Q)$ gravity possesses the distinct geometric formulation, where gravitational dynamics are encoded in spacetime influenced by non-Riemannian geometry (non-metricity), a systematic Bayesian inference of its model parameters using NS observables remains largely unexplored. This motivates the present work, in which NSs data are employed to directly constrain the parameter space of $f(Q)$ gravity beyond cosmological tests. In this work, we address this gap by performing a comparative analysis of NSs in the strong-gravity regime within the framework of $f(Q)$ gravity, considering three representative models - linear, logarithmic, and exponential. To minimize uncertainties arising from dense-matter physics, we adopt the realistic DDME2 EoS [58, 59], which is consistent with nuclear and astrophysical constraints. Most importantly, for the first time in literature of $f(Q)$ gravity, we have employed the Bayesian inference framework to constrain the free model parameters and compare their predictions for NS properties with observational data from the NICER. This approach enables a systematic assessment of the viability of different $f(Q)$ models in the strong-field regime, highlighting the role of NSs as powerful probes of symmetric teleparallel gravity beyond cosmological scales. Therefore, our paper is organized as follows:

The organization of this paper is as follows. In Sec. II, we briefly outline the geometrical formalism of $f(Q)$ gravity. The modified Tolman–Oppenheimer–Volkoff (TOV) equations governing the neutron-star structure in $f(Q)$ gravity are derived in Sec. III. In Sec. IV, we introduce the three representative $f(Q)$ models considered in this study. The numerical methodology for solving the modified TOV equations and the Bayesian inference framework used for parameter estimation are presented in Sects. V and VI, respectively. Our results, including a comparative analysis of the different models, are discussed in Sec. VII. Finally, we summarize our findings and present concluding remarks in Sec. VIII.

II. GEOMETRY OF $f(Q)$ GRAVITY

In the context of metric-affine geometry, a spacetime is characterized by the triplet $(\mathcal{M}, g_{\mu\nu}, \Gamma_{\mu\nu}^\alpha)$, where \mathcal{M} denotes a four-dimensional differentiable manifold, $g_{\mu\nu}$ is the metric tensor (with signature $(-, +, +, +)$ or $(+, -, -, -)$), and $\Gamma_{\mu\nu}^\alpha$ represents a general affine connection, independent of the metric. This framework allows for a more general geometric structure than that of standard Riemannian geometry, as it permits torsion and non-metricity in addition to curvature.

The affine connection defines a covariant derivative that governs how vectors and covectors change under parallel transport. Explicitly, for a vector V^α and a covector V_α , the covariant derivatives are defined by:

$$\nabla_\mu V^\alpha = \partial_\mu V^\alpha + \Gamma_{\mu\lambda}^\alpha V^\lambda, \quad (1)$$

$$\nabla_\mu V_\alpha = \partial_\mu V_\alpha - \Gamma_{\mu\alpha}^\lambda V_\lambda. \quad (2)$$

A general affine connection $\Gamma_{\mu\nu}^\alpha$ can be decomposed into three independent components [23]:

$$\Gamma_{\mu\nu}^\alpha = \mathring{\Gamma}_{\mu\nu}^\alpha + K_{\mu\nu}^\alpha + L_{\mu\nu}^\alpha, \quad (3)$$

where $\mathring{\Gamma}_{\mu\nu}^\alpha$ is the Levi-Civita connection or widely known as the Christoffel symbol and defined by,

$$\mathring{\Gamma}_{\mu\nu}^\alpha = \frac{1}{2} g^{\alpha\lambda} (\partial_\mu g_{\nu\lambda} + \partial_\nu g_{\mu\lambda} - \partial_\lambda g_{\mu\nu}). \quad (4)$$

Moreover, $K_{\mu\nu}^\alpha$ is the contortion tensor associated with torsion tensor defined by $T_{\mu\nu}^\alpha := 2\Gamma_{[\mu\nu]}^\alpha$ from which the contortion tensor is defined as,

$$K_{\mu\nu}^\alpha := \frac{1}{2} (T_{\mu\nu}^\alpha + T_{\mu\nu}^\alpha + T_{\mu\nu}^\alpha). \quad (5)$$

Finally, the disformation tensor is given by

$$L_{\mu\nu}^\alpha := \frac{1}{2} (Q_{\mu\nu}^\alpha - Q_{\mu\nu}^\alpha - Q_{\mu\nu}^\alpha), \quad (6)$$

in terms of the non-metricity tensor

$$Q_{\alpha\mu\nu} = \nabla_\alpha g_{\mu\nu} = \partial_\alpha g_{\mu\nu} - \Gamma_{\alpha\mu}^\beta g_{\beta\nu} - \Gamma_{\alpha\nu}^\beta g_{\mu\beta}. \quad (7)$$

Symmetric teleparallel gravity (STG) describes a class of non-metric gravity theories in which both curvature and torsion of the affine connection vanish, so gravity is encoded purely by non-metricity, i.e.,

$$R_{\mu\nu\sigma}^\lambda = 0 \quad \text{and} \quad T_{\mu\nu}^\alpha = 0. \quad (8)$$

Therefore, in STG the connection reduces to

$$\Gamma_{\mu\nu}^\alpha = \{\alpha\}_{\mu\nu} + L_{\mu\nu}^\alpha. \quad (9)$$

Next, we introduce the nonmetricity conjugate:

$$P^{\alpha\mu\nu} = -\frac{1}{4}Q^{\alpha\mu\nu} + \frac{1}{2}Q^{(\mu\nu)\alpha} + \frac{1}{4}(Q^\alpha - \tilde{Q}^\alpha)g^{\mu\nu}, \quad (10)$$

where its two independent traces are given by,

$$Q_\alpha = Q_{\alpha\mu}^\mu, \text{ and } \tilde{Q}_\alpha = Q^\mu_{\alpha\mu}. \quad (11)$$

Finally, the nonmetricity scalar is defined as:

$$Q = -Q_{\alpha\mu\nu}P^{\alpha\mu\nu}. \quad (12)$$

Incorporating constraints via Lagrange multipliers, the modified Einstein-Hilbert action in $f(Q)$ gravity is given by [60]:

$$S = \int \sqrt{-g} d^4x \left[\frac{1}{2}f(Q) + \lambda_\alpha^{\beta\mu\nu}R^\alpha_{\beta\mu\nu} + \lambda_\alpha^{\mu\nu}T^\alpha_{\mu\nu} + \mathcal{L}_m \right], \quad (13)$$

where g denotes the determinant of the spacetime metric $g_{\mu\nu}$, $f(Q)$ is an arbitrary function of the nonmetricity scalar Q , $\lambda_\alpha^{\beta\mu\nu}$ and $\lambda_\alpha^{\mu\nu}$ serve as Lagrange multipliers, and \mathcal{L}_m is the Lagrangian density corresponding to matter.

Changing the action (13) with respect to the metric tensor, one arrives at the following field equation:

$$\begin{aligned} -T_{\mu\nu} &= \frac{2}{\sqrt{-g}}\nabla_\alpha(\sqrt{-g}f_Q P^\alpha_{\mu\nu}) + \frac{1}{2}g_{\mu\nu}f \\ &+ f_Q(P_{\mu\alpha\beta}Q_\nu^{\alpha\beta} - 2Q_{\alpha\beta\mu}P^{\alpha\beta}_\nu), \end{aligned} \quad (14)$$

Here, the subscript Q implies the differentiation of $f(Q)$ with respect to Q , that is, $f_Q \equiv \partial_Q f(Q)$. The standard definition of the energy-momentum tensor given by,

$$T_{\mu\nu} \equiv -\frac{2}{\sqrt{-g}}\frac{\delta(\sqrt{-g}\mathcal{L}_m)}{\delta g^{\mu\nu}}. \quad (15)$$

As discussed in [61], the equation of motion given in Eq.(14) can be rewritten in a covariant form, similar to the standard Einstein gravitational field equations, as

$$f_Q \mathring{G}_{\mu\nu} + \frac{1}{2}g_{\mu\nu}(f_Q Q - f) + 2f_{QQ}(\partial_\lambda Q)P^\lambda_{\mu\nu} = T_{\mu\nu}, \quad (16)$$

where $\mathring{G}_{\mu\nu} = \mathring{R}_{\mu\nu} - \frac{1}{2}\mathring{R}g_{\mu\nu}$ denotes the Einstein tensor constructed from the Levi-Civita connection. Written in this form, the equation clarifies the role of diffeomorphism invariance in the theory. In the special case of STGR, where $f(Q) = Q$, the left-hand side of Eq. (16) reduces identically to the Einstein tensor, which depends only on the metric. Consequently, the choice of affine connection does not influence the metric dynamics, in agreement with the discussion in the previous section. In contrast, for general $f(Q)$ models with nonlinear

dependence on Q , the affine connection explicitly enters the field equations and therefore affects the evolution of the metric.

Upon variation of Eq. (13) with respect to the affine connection, one can get:

$$\nabla_\rho \lambda_\alpha^{\nu\mu\rho} + \lambda_\alpha^{\mu\nu} = \sqrt{-g}f_Q P^\alpha_{\mu\nu} + H_\alpha^{\mu\nu}, \quad (17)$$

where the hypermomentum tensor is defined as:

$$H_\alpha^{\mu\nu} = -\frac{1}{2}\frac{\delta\mathcal{L}_m}{\delta\Gamma_{\mu\nu}^\alpha}. \quad (18)$$

Using the fact that the Lagrange multipliers are antisymmetric in μ and ν , Eq. (17) simplifies to:

$$\nabla_\mu \nabla_\nu (\sqrt{-g}f_Q P^{\mu\nu}) = 0. \quad (19)$$

Assuming the hypermomentum contribution satisfies $\nabla_\mu \nabla_\nu H_\alpha^{\mu\nu} = 0$ (for further explanation, readers may look into Ref. [60]), this reduces to:

$$\nabla_\mu \nabla_\nu (\sqrt{-g}f_Q P^{\mu\nu}) = 0. \quad (20)$$

Next, in the absence of both curvature and torsion, the affine connection is expressible via [21]:

$$\Gamma_{\mu\nu}^\alpha = \left(\frac{\partial x^\alpha}{\partial \xi^\lambda} \right) \partial_\mu \partial_\nu \xi^\lambda. \quad (21)$$

Furthermore, A convenient coordinate system called the coincident gauge may be adopted such that the affine connection vanishes identically, i.e., $\Gamma_{\mu\nu}^\alpha = 0$. Under this condition, the nonmetricity tensor becomes:

$$Q_{\alpha\mu\nu} = \partial_\alpha g_{\mu\nu}, \quad (22)$$

greatly streamlining calculations by making the metric the sole dynamical variable. However, this choice restricts diffeomorphism invariance, an issue only circumvented in STGR [62].

III. MODIFIED TOV IN $f(Q)$ GRAVITY

To describe the stellar structure, we consider the general form of a static, spherically symmetric spacetime given by the metric,

$$ds^2 = -e^{\nu(r)}dt^2 + e^{\lambda(r)}dr^2 + r^2d\Omega^2, \quad (23)$$

where $d\Omega^2 = d\theta^2 + \sin^2\theta d\phi^2$ represents the metric on the unit 2-sphere. $\nu(r)$ and $\lambda(r)$ represents the metric potential along the $-tt$ and $-rr$ direction. In this spherically symmetric case, we model the matter content

as an isotropic fluid whose energy-momentum tensor takes the form of

$$T_{\mu\nu} = (\varepsilon + p) u_\mu u_\nu + p g_{\mu\nu}. \quad (24)$$

Here, u_μ is the fluid's four-velocity, satisfying the orthogonality and normalization conditions: $u^\mu u_\mu = -1$, and $u^\mu v_\mu = 0$. The functions $\varepsilon(r)$, $p(r)$ denote the energy density and radial pressure of the fluid respectively.

From the modified field equations corresponding to the isotropic fluid and the metric above, the independent components of the field equations can be derived as:

$$\varepsilon = \frac{f}{2} - f_Q \left(Q + \frac{1}{r^2} + \frac{e^{-\lambda}}{r} (\nu' + \lambda') \right), \quad (25)$$

$$p = -\frac{f}{2} + f_Q \left(Q + \frac{1}{r^2} \right), \quad (26)$$

$$p = -\frac{f}{2} + f_Q \left\{ \frac{Q}{2} - e^{-\lambda} \left[\frac{\nu''}{2} + \left(\frac{\nu'}{4} + \frac{1}{2r} \right) (\nu' - \lambda') \right] \right\}, \quad (27)$$

$$0 = \frac{\cot \theta}{2} Q' f_{QQ}. \quad (28)$$

Using this line element in the context of symmetric teleparallel gravity, the nonmetricity scalar Q becomes a function of the radial coordinate and is given by

$$Q(r) = -\frac{2e^{-\lambda}}{r} \left(\nu' + \frac{1}{r} \right), \quad (29)$$

where the prime denotes a derivative with respect to r .

Upon substituting the expression for Q from Eq. (29) into the equations of motion Eq. (25) and Eq. (26), the modified version of the TOV equation in $f(Q)$ gravity takes the form:

$$\begin{aligned} p' + \frac{\nu'}{2} (\varepsilon + p) &= f_Q \frac{e^{-\lambda}}{2r} \left[\frac{2}{r} (\nu' + \lambda') - \nu' (\nu' - \lambda') \right. \\ &\quad \left. + \frac{4}{r^2} (1 - e^\lambda) - 2\nu'' \right] = 0. \end{aligned} \quad (30)$$

By solving Eqs. (25)–(27) for a specific functional form of $f(Q)$, together with appropriate boundary conditions, the metric functions $\nu(r)$ and $\lambda(r)$ can be determined. As an illustrative case, for vacuum solutions with $T_{\mu\nu} = 0$, Eqs. (25) and (26) imply the relation

$$\nu'(r) + \lambda'(r) = 0. \quad (31)$$

In general, Eqs. (25)–(27) can be reformulated as a system of modified TOV equations in the framework of $f(Q)$ gravity. These equations describe the internal structure of neutron stars and are supplemented by the continuity equation arising from the conservation of the

energy-momentum tensor $T_{\mu\nu}$, given by

$$p' + \frac{\nu'}{2} (\varepsilon + p) = 0, \quad (32)$$

$$\lambda' = \frac{-kr(\rho + p)e^\lambda - \nu'}{f(Q)}, \quad (33)$$

$$\begin{aligned} \nu'' &= \frac{1}{2rf_Q} \left[2rQf_Qe^\lambda - (r\nu' + 2)(\nu' - \lambda')f_Q \right. \\ &\quad \left. - 2(2kp + f(Q))re^\lambda \right]. \end{aligned} \quad (34)$$

By specifying an EoS and providing suitable initial conditions for the metric functions $\nu(r)$ and $\lambda(r)$, as well as for the energy density ε and pressure p , the stellar structure of NSs can be fully determined in $f(Q)$ gravity. In the particular limit $f(Q) = -Q$, Eqs. (25)–(27) reduce to the standard field equations of GR, and the corresponding GR solutions are recovered (see Appendix A). These equations therefore allow for the computation of NS configurations for various $f(Q)$ gravity models.

IV. $f(Q)$ MODELS

In this work, we investigate the internal structure of NSs in the context of $f(Q)$ gravity by considering three representative functional forms, namely linear, logarithmic, and exponential models. These formulations extend the standard gravitational action through both linear and nonlinear dependencies on the nonmetricity scalar Q , leading to modified field equations that govern stellar equilibrium. A systematic examination of these models allows us to assess how deviations from GR influence the macroscopic characteristics of NSs.

A. Linear Model

To investigate the role of different functional forms of $f(Q)$, we first focus on the linear model [23],

$$f(Q) = \alpha \left(\frac{Q}{Q_0} \right) + \beta, \quad (35)$$

which emerges directly from Eq. (28) upon imposing the condition $f_{QQ} = 0$. This constraint restricts the gravitational action to depend linearly on the nonmetricity scalar Q . Here, α and β are constant parameters that characterize deviations from GR, while Q_0 is a constant with dimensions of $[\text{length}]^{-2}$, introduced to ensure that the argument of the function is dimensionless.

The linear $f(Q)$ model constitutes the minimal extension of STG and is exactly reduced to GR

for $\alpha = -1$ and $\beta = 0$. Owing to the absence of higher-order derivatives, the resulting field equations remain second order, ensuring mathematical consistency and freedom from additional dynamical degrees of freedom. Consequently, this model provides a well-controlled theoretical baseline for isolating leading-order gravitational modifications and serves as a natural reference against which nonlinear $f(Q)$ models can be systematically assessed in the context of NS structure.

B. Logarithmic Model

We now turn to a logarithmic form of the $f(Q)$ function, which introduces scale-dependent corrections to the gravitational action and has been widely studied in [24]. The model is specified as

$$f(Q) = -Q + \alpha \ln \left[\beta \left(\frac{Q}{Q_0} \right) \right], \quad (36)$$

where α and β are constant parameters controlling the magnitude and scale of the logarithmic correction, and Q_0 is a constant with dimensions of $[\text{length}]^{-2}$ introduced to ensure a dimensionless argument of the logarithm. In the limit $\alpha \rightarrow 0$, the logarithmic contribution vanishes and the theory is reduced to the symmetric teleparallel formulation equivalent to GR.

The logarithmic $f(Q)$ model is motivated by its ability to introduce controlled scale-dependent deviations from GR. Logarithmic corrections naturally emerge in effective field theories and quantum-inspired gravity [63], encoding running gravitational effects that remain negligible in the weak-field limit while becoming relevant in intermediate and strong-field regimes, such as those encountered in compact objects.

From a cosmological standpoint, logarithmic $f(Q)$ models have been widely applied to study late-time cosmic acceleration, dynamical dark energy, and phase-space stability [27]. These properties provide a compelling motivation to investigate their implications for NS interiors, where strong gravity may amplify scale-dependent effects.

C. Exponential Model

Finally, we consider an exponential form of the $f(Q)$ function, which introduces nonlinear corrections to the gravitational action and has been widely explored in the

literature [26]. The model is defined as

$$f(Q) = -Q + \alpha Q_0 \left[1 - \exp \left(-\beta \sqrt{\frac{Q}{Q_0}} \right) \right], \quad (37)$$

where α and β are dimensionless parameters characterizing the strength and scale of deviations from GR, and Q_0 is a constant with dimensions of $[\text{length}]^{-2}$ introduced to render the argument of the exponential dimensionless. In the limit $\beta \rightarrow 0$, the exponential correction vanishes and the theory reduces to the symmetric teleparallel formulation equivalent to GR.

The exponential model is physically motivated by its ability to generate smooth and controlled deviations from GR while remaining well behaved in both the weak and strong field regimes [25]. The exponential suppression ensures that nonlinear corrections become significant only above a characteristic scale set by Q_0 , allowing the theory to recover GR at low curvatures while permitting appreciable modifications in high-density environments. Such properties make this model particularly attractive for studying compact objects, where strong gravitational fields can amplify deviations from standard gravity.

Beyond astrophysical applications, exponential $f(Q)$ models have been extensively employed in cosmological contexts, including inflationary dynamics, constraints from big bang nucleosynthesis, and phase-space analyses of cosmic evolution [64]. These successes motivate their application to NS interiors, where they provide a theoretically consistent framework to probe the impact of nonlinear nonmetricity effects on stellar structure.

V. BOUNDARY CONDITIONS AND EQUATION OF STATE

For each $f(Q)$ model, we compute the interior and exterior structure of neutron stars by numerically integrating the modified TOV equations. The system consists of coupled ordinary differential equations for the enclosed mass $m(r)$, the metric functions $\lambda(r)$ and $\nu(r)$, and the pressure $p(r)$. These equations are solved using a fourth-order Runge-Kutta (RK4) scheme.

The integration is initiated at the stellar center, where regularity imposes the boundary conditions

$$m(0) = 0, \quad \lambda(0) = 0, \quad \nu'(0) = 0. \quad (38)$$

The central pressure p_c is determined from a realistic tabulated equation of state (EoS). In this work, we adopt the density-dependent relativistic mean-field DDME2 EoS [59], which provides a consistent relation between

pressure and energy density. The central energy density ε_c is varied over the range 100–1700 MeV fm^{−3}, corresponding to several times the nuclear saturation density.

For a given ε_c , the modified TOV equations are integrated radially outward with a fixed step size $\Delta r = 0.01$ km until the pressure vanishes, $p(R) = 0$, which defines the stellar surface at radius R . The total gravitational mass is then obtained as $M = m(R)$. To ensure a physically consistent global solution, the central value of the metric function $\nu(r_0)$ is determined using a shooting method: the trial value of $\nu(r_0)$ is iteratively adjusted until the interior solution matches smoothly to the exterior Schwarzschild spacetime at the surface, satisfying

$$e^{\nu(R)} = e^{-\lambda(R)} = 1 - \frac{2M}{R}. \quad (39)$$

Repeating this procedure over the full range of central energy densities yields the mass–radius relation for each $f(Q)$ model. This allows us to systematically assess the impact of nonmetricity-induced corrections on neutron-star structure and to compare the resulting configurations with observational constraints.

VI. BAYESIAN ESTIMATION

A Bayesian approach allows one to perform a detailed statistical analysis of the parameters of a model for a given set of data. This approach is based on *Bayes' theorem*. It combines prior knowledge with fit data to produce the *posterior probability* distribution for model parameters. This posterior distribution effectively quantifies the probability of every possible parameter hypothesis. From this, we can study individual parameter distributions and examine correlations between them. For a given dataset \mathcal{D} and a hypothesis $H(\theta)$, *Bayes' theorem* is expressed as

$$P(\theta|\mathcal{D}, H) = \frac{\mathcal{L}(\mathcal{D}|\theta, H)P(\theta|H)}{P(\mathcal{D}|H)}.$$

The components of *Bayes' theorem* are defined as follows:

- **Posterior probability** $P(\theta|\mathcal{D}, H)$: The updated probability of parameters θ after observing data \mathcal{D} within the model H .
- **Likelihood** $\mathcal{L}(\mathcal{D}|\theta, H)$: The probability of observing the data \mathcal{D} given specific parameter values θ under the hypothesis H .
- **Prior probability** $P(\theta|H)$: The initial probability assigned to θ before seeing the data, based on existing knowledge or assumptions.

- **Marginal likelihood (evidence)** $P(\mathcal{D}|H)$: A normalizing constant representing the probability of the data \mathcal{D} under H , averaged over all possible values of θ .

A. Likelihood

In Bayesian analysis, the likelihood function quantifies the probability of the observed data for a given set of model parameters θ . It can be computed for a given posterior distributions from astrophysical observations as follows:

X-ray observations (NICER): X-ray observations of NS hot spots by the NICER mission have given some of the strongest constraints on NS masses and radii. The X-ray measurements provide the mass and radius of individual pulsars, both isolated and in binaries. These measurements offer a direct way to study the dense-matter EoS.

The main NICER results come from two key pulsars. For PSR J0030+0451 (at a canonical mass), mass–radius posteriors were published independently by two groups: Riley *et al.* [65]¹ and Miller *et al.* [66]². For PSR J0740+6620 (near the maximum mass), similar posteriors were released by Riley *et al.* [40]³ and Miller *et al.* [39]⁴. Recently, NICER has provided additional mass–radius measurements for other pulsars such as PSRJ0437+4715 from Choudhury *et al.* [67]⁵ and PSRJ0614+3329 from Mauviard *et al.* [68]⁶.

For the NICER mass–radius observations, the likelihood is formally expressed by marginalizing over the stellar mass:

$$\mathcal{L}^{\text{NICER}}(\boldsymbol{\theta}_{f(Q)}) \equiv P(d_{\text{X-ray}}|\boldsymbol{\theta}_{f(Q)}) = \int_{M_l}^{M_u} dm P(m|\boldsymbol{\theta}_{f(Q)}) P(d_{\text{X-ray}}|m, R(m, \boldsymbol{\theta}_{f(Q)})). \quad (40)$$

Here, M_l denotes the lower mass bound, taken to be $1 M_\odot$, and $M_u(\boldsymbol{\theta}_{f(Q)})$ represents the maximum NS mass obtained by solving the modified TOV equations [69, 70] for a given set of $f(Q)$ model parameters $\boldsymbol{\theta}_{f(Q)}$, assuming the DDME2 EoS.

Suppose there are three statistically independent datasets A , B , and C , with corresponding Bayesian

¹ <https://zenodo.org/records/8239000>

² <https://zenodo.org/record/3473466>

³ <https://zenodo.org/records/4697625>

⁴ <https://zenodo.org/records/4670689>

⁵ <https://zenodo.org/records/13766753>

⁶ <https://zenodo.org/records/15603406>

likelihoods $\mathcal{L}^A(\boldsymbol{\theta})$, $\mathcal{L}^B(\boldsymbol{\theta})$, and $\mathcal{L}^C(\boldsymbol{\theta})$, where $\boldsymbol{\theta}$ denotes the model parameters. Under the assumption of statistical independence, the joint likelihood is given by

$$\mathcal{L}(\boldsymbol{\theta}) = \prod_{i=A,B,C} \mathcal{L}^i(\boldsymbol{\theta}). \quad (41)$$

B. Bayes Factor

A *Bayes factor* (BF) measures the strength of evidence provided by the data in favor of one hypothesis H_1 over another H_2 . It is defined as:

$$\text{BF}_{12} = \frac{P(D|H_1)}{P(D|H_2)}, \quad (42)$$

where,

- $P(D|H_1)$ is the likelihood of the data D under hypothesis H_1 .
- $P(D|H_2)$ is the likelihood of the data D under hypothesis H_2 .

1. Log of the Bayes Factor

Taking the *logarithm* of the Bayes factor provides a more practical scale for interpretation and calculation. The log Bayes factor is:

$$\ln(\text{BF}_{12}) = \ln \left(\frac{P(D|H_1)}{P(D|H_2)} \right), \quad (43)$$

This transformation provides a more practical scale for quantifying the strength of evidence that favors one hypothesis.

2. Interpretation of the Bayes Factor

To assess the strength of evidence, the values of the Bayes factor are often assessed using the following conventional scale [71, 72]:

- $\ln(\text{BF}) > 1$: Strong evidence for hypothesis H_1 .
- $0 < \ln(\text{BF}) < 1$: Weak to moderate evidence for hypothesis H_1 .
- $\ln(\text{BF}) = 0$: No evidence for either hypothesis.
- $-1 < \ln(\text{BF}) < 0$: Weak to moderate evidence for hypothesis H_2 .
- $\ln(\text{BF}) < -1$: Strong evidence for hypothesis H_2 .

VII. RESULTS

We investigate the impact of observational data on NS properties mass, radius, tidal deformability, and compactness using a set of $f(Q)$ models: the Linear, Logarithmic, and Exponential forms detailed in Sec. IV. These models are constrained within a Bayesian framework using NICER mass-radius posteriors. To assess the flexibility of each $f(Q)$ model, we adopt the DDME2 hadronic EoS as a baseline. In Fig. 1, we plot the energy density (ϵ) (left), pressure (P) (middle), and speed of sound (c_s^2) (right) as a function of baryon density for DDME2. The prior distributions for the model parameters are listed in Table I.

TABLE I: Uniform priors on the $f(Q)$ model parameters.

Parameter	Prior
α	$[-15, 15]$
β	$[-3, 5]$
Q_0	$[-1, 1]$

A. Posterior distribution of $f(Q)$ model parameters and NS Properties

TABLE II: The median values and associated 68% (90%) uncertainties for the parameters from their marginalized posterior distributions. The results are obtained for Linear, Logarithmic and Exponential models.

Models	Parameters		
	α	β	Q_0
Linear	$0.15^{+0.71(0.87)}_{-0.99(1.16)}$	$2.11^{+1.62(2.51)}_{-1.18(1.70)}$	$-0.16^{+0.96(1.09)}_{-0.67(0.78)}$
Logarithmic	$1.55^{+1.18(2.41)}_{-0.87(1.33)}$	$1.11^{+2.52(3.45)}_{-3.02(3.77)}$	$-0.26^{+0.86(1.12)}_{-0.50(0.66)}$
Exponential	$-5.18^{+2.97(3.89)}_{-5.52(8.31)}$	$2.64^{+1.58(2.15)}_{-1.71(2.14)}$	$-0.35^{+0.20(0.28)}_{-0.36(0.54)}$

The corner plots for the marginalized posterior distributions for $f(Q)$ model parameters of Linear (red), Logarithmic (purple), and Exponential (green) models are shown in Fig. 2. The marginalized one-dimensional posterior distributions for the parameters are displayed along the diagonals of the corner plots. The median values of the parameters and their uncertainties 2σ ,

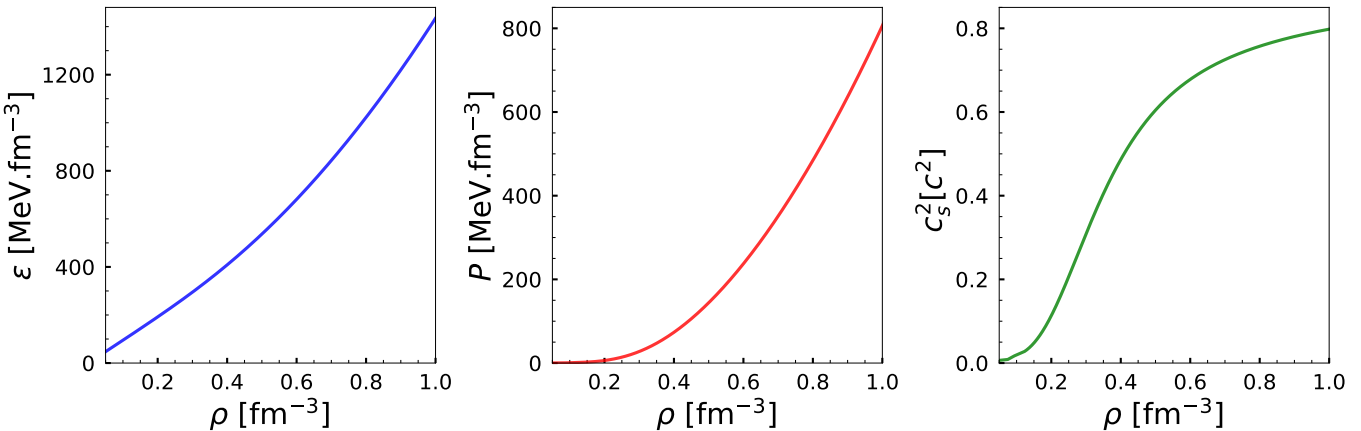


FIG. 1: The energy density (ϵ) (in $\text{MeV} \cdot \text{fm}^{-3}$) (left panel), pressure (P) (in $\text{MeV} \cdot \text{fm}^{-3}$) (middle panel), and speed of sound (c_s^2) (in c^2) (right panel) as a function of baryon density (ρ) (in fm^{-3}) for DDME2.

TABLE III: Similar to Table II, but, for the NS properties, namely the tidal deformability ($\Lambda_{1.4}$), radii ($R_{1.4}$ and $R_{2.07}$) and maximum mass (M_{max}) .

Models	NS Properties			
	$\Lambda_{1.4}$	$R_{1.4}$	$R_{2.07}$	M_{max}
Linear	$138.55^{+59.62(133.04)}_{-27.87(37.99)}$	$11.15^{+0.45(0.81)}_{-0.29(0.41)}$	$11.68^{+0.39(0.65)}_{-0.40(0.87)}$	$2.29^{+0.35(0.57)}_{-0.20(0.29)}$
Logarithmic	$135.82^{+64.59(179.65)}_{-23.33(32.21)}$	$11.09^{+0.48(1.05)}_{-0.22(0.32)}$	$12.08^{+0.36(0.65)}_{-0.25(0.42)}$	$2.36^{+0.28(0.42)}_{-0.23(0.32)}$
Exponential	$156.95^{+84.02(177.68)}_{-41.73(55.77)}$	$11.27^{+0.53(0.97)}_{-0.36(0.52)}$	$11.76^{+0.50(0.83)}_{-0.36(0.50)}$	$2.29^{+0.11(0.16)}_{-0.13(0.21)}$

drawn from the marginalized posterior distributions, are shown. The vertical lines indicate the 68% confidence interval of the parameters. We also plot the 2D confidence ellipses along with the off-diagonal corner plots, corresponding to the credible intervals 1σ , 2σ , and 3σ . The shapes and orientations of these ellipses indicate the presence or absence of correlations between the parameters. The correlation between α and Q_0 is strong in the Lin case ($r \sim -0.99$), moderate in the Exponential case ($r \sim -0.64$) and negligible in the Logarithmic case ($r \sim -0.14$). A strong correlation between β and Q_0 is found only for the Logarithmic model ($r \sim -0.80$). The median values of the model parameters and the corresponding confidence intervals of 68% (90%) obtained from the marginalized posterior distributions are listed in Table II. The Exponential model has a wider range of parameter distributions than the others, while the Lin model has the narrowest range. The Q_0 parameter is constrained the tightest across all models (uncertainties ~ 0.2 – 1.1), especially in the Exponential model where it shows the smallest relative error, suggesting it is the best-constrained

by the NICER data. The Logarithmic model shows the largest parameter uncertainties, particularly for β ($1.11^{+2.52(3.45)}_{-3.02(3.77)}$), indicating weaker constraints or greater degeneracy within this model. The parameter α differs significantly between models: positive for Linear and Logarithmic (~ 0.15 , 1.55) but negative for Exponential (-5.18), highlighting how the functional form of $f(Q)$ changes the preferred gravity modification.

We have obtained the distributions of the tidal deformability $\Lambda_{1.4}$, radii $R_{1.4}$ (km) and $R_{2.07}$ (km) and the maximum mass M_{max} (M_\odot) using the posterior distributions for the parameters corresponding to the Linear, Logarithmic and Exponential models as listed in Table II. The corner plots for these NS properties are shown in Fig. 3. The same as Fig. 2, the vertical lines, median values with 2σ uncertainties, and 2D confidence ellipses along the off-diagonal line are shown. It is clear from the off-diagonal graphs that $\Lambda_{1.4}$ is strongly correlated with $R_{1.4}$ for all models ($r \sim 0.96$). In the case of the Exponential model, all quantities are strongly correlated with each other ($r \sim 0.95$). The maximum mass is found to be uncorrelated with other

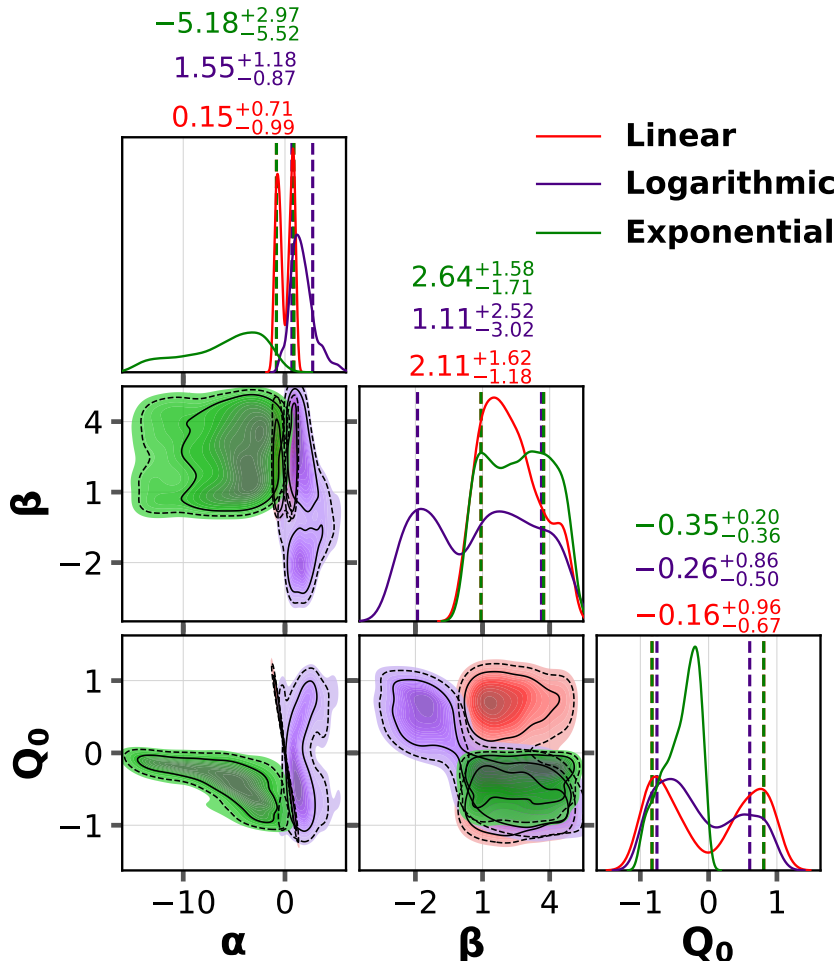


FIG. 2: The marginalized posterior distributions of the $f(Q)$ model parameters, obtained through Bayesian inference, for Linear (red), Logarithmic (purple), and Exponential (green) models. The vertical lines indicate the 68% confidence interval of the parameters. The confidence ellipses for two-dimensional posterior distributions are plotted with 1σ , 2σ and 3σ confidence intervals.

NS properties in Linear and Logarithmic cases. We have summarized the median values of the properties of NS together with 68% (90%) confidence intervals in Table III. It shows how different MG theories affect these astrophysical quantities. The Logarithmic model predicts the highest maximum mass ($2.36^{+0.28}_{-0.23}$) while the Exponential model shows the widest uncertainty ranges for most properties, particularly for $\Lambda_{1.4}$, indicating different constraint sensitivities. The radii predictions for $R_{1.4}$ and $R_{2.07}$ are remarkably similar for all models, differing by less than ~ 0.4 km in the median values. This suggests that within these $f(Q)$ models, the predicted radius does not change significantly with mass in this range.

Figure 4 displays the 95% confidence bands for

the M – R (left panel), M – Λ (middle panel), and M – M/R (right panel) relations for the Linear (magenta), Logarithmic (purple), and Exponential (orange) models. All NICER observational constraints incorporated in the Bayesian framework are also shown. The M – R curves for all models pass through the centers of the observational bands, indicating that the Bayesian inference successfully reproduces the observed data. The Exponential model exhibits the widest confidence band, particularly in the 1 – $2 M_\odot$ mass range, consistent with its larger parameter uncertainties (see Table II). In contrast, the Linear model shows the narrowest band, reflecting its tighter parameter constraints. The Logarithmic model yields broader distributions above $2M_\odot$, suggesting a greater capacity to produce stiffer high-mass M – R

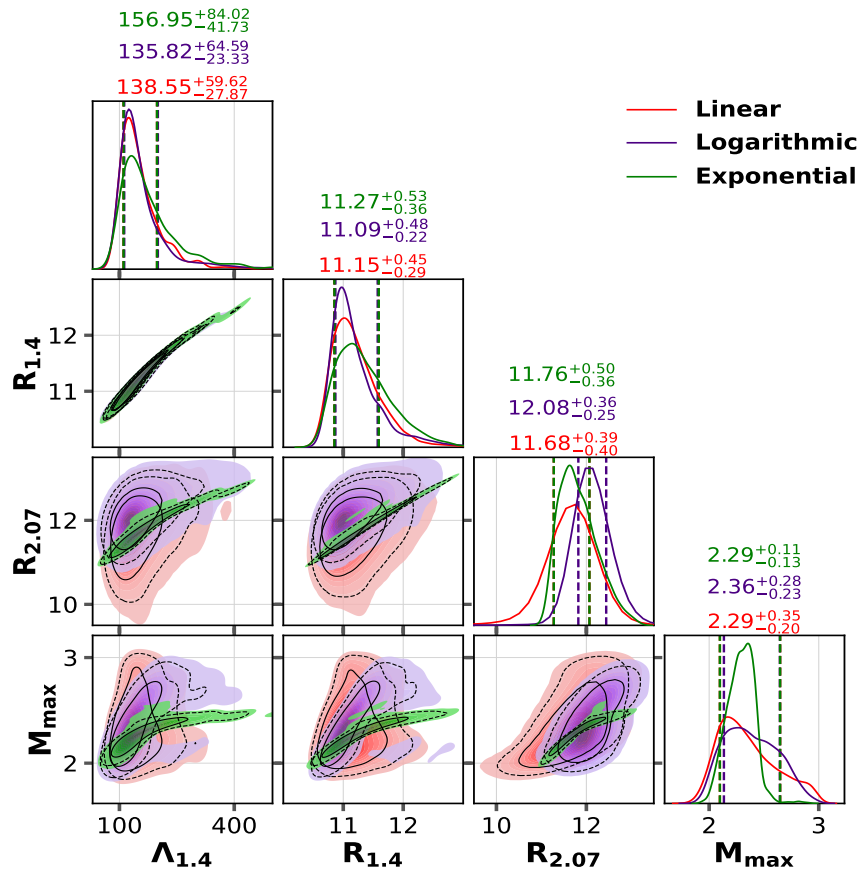


FIG. 3: Corner plots for the marginalized posterior distributions (salmon) of the tidal deformability $\Lambda_{1.4}$, radii $R_{1.4}$ (km) and $R_{2.07}$ (km) and the maximum mass M_{max} (M_{\odot}) for Linear (red), Logarithmic (purple), and Exponential (green).

configurations. For the $M - \Lambda$ distributions, all three models follow similar trends. In terms of compactness, the Linear model reaches higher M/R values than the others at a given mass. The different compactness trends between models highlight how each $f(Q)$ functional form alters the mass-radius relation, particularly in the high-density regime.

The Pearson's correlation coefficients among all $f(Q)$ model parameters (α , β , and Q_0) and the NS (NS) properties ($\Lambda_{1.4}$, $R_{1.4}$, $R_{2.07}$, and M_{max}) are shown in Fig. 5. The left, middle, and right panels correspond to the Linear, Logarithmic, and Exponential models, respectively. In the Linear model, β is strongly correlated with the radius and tidal deformability at the canonical mass, with correlation coefficients of -0.79 and -0.70 , respectively. This indicates that β plays a key role in defining the canonical NS properties in the Linear case. In the Logarithmic model, α is moderately correlated with these canonical properties. In contrast, for the Exponential model, no strong correlation is

found between individual parameters and NS properties, suggesting that the parameters **collectively** relate to NS properties.

B. Model Comparison

TABLE IV: The logarithmic Bayes factor for all $f(Q)$ models considered for this analysis. Here we consider Exponential as H_2 hypothesis always and other models as H_1 to compute $\ln(\text{BF}_{12})$ using Eq. (43).

Model	$\ln(\text{BF}_{12})$
Linear	-1.28
Logarithmic	-0.35

Since we use a large number of $f(Q)$ models for this analysis, it would be good to compare these models statistically using the Bayes factor as discussed in

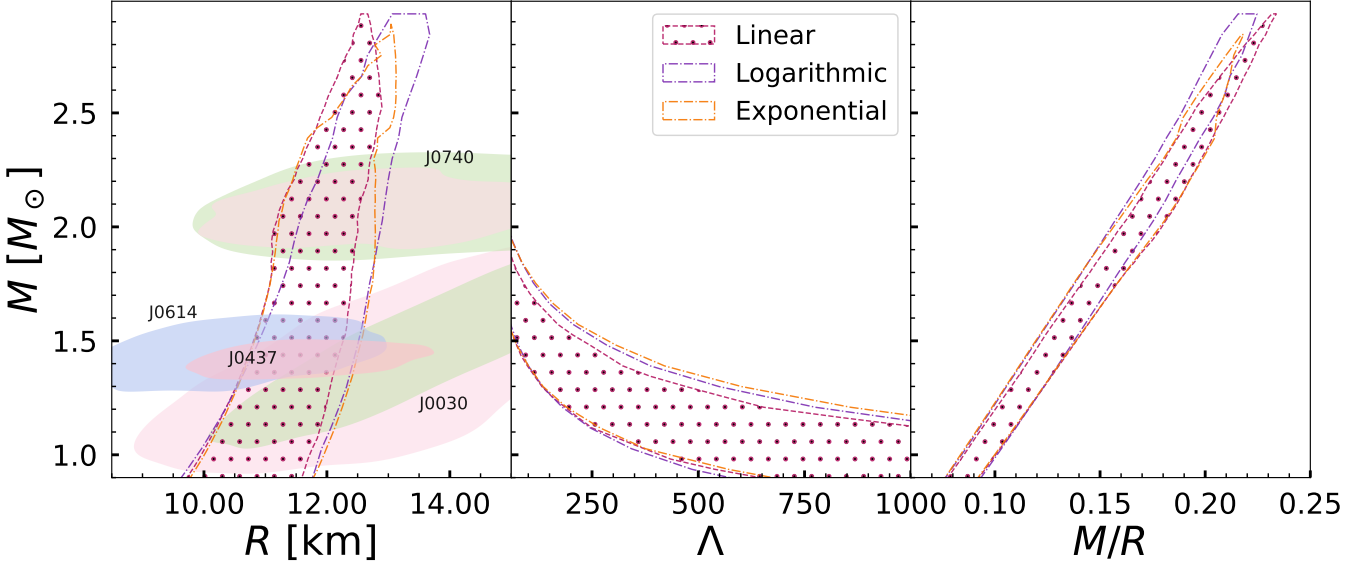


FIG. 4: The 95% confidence interval distributions for the radius R (km) (left panel), tidal deformability Λ (middle panel) and compactness M/R (right panel) as a function of NS mass M (M_\odot). The astrophysical observations incorporated in the Bayesian framework are also shown.

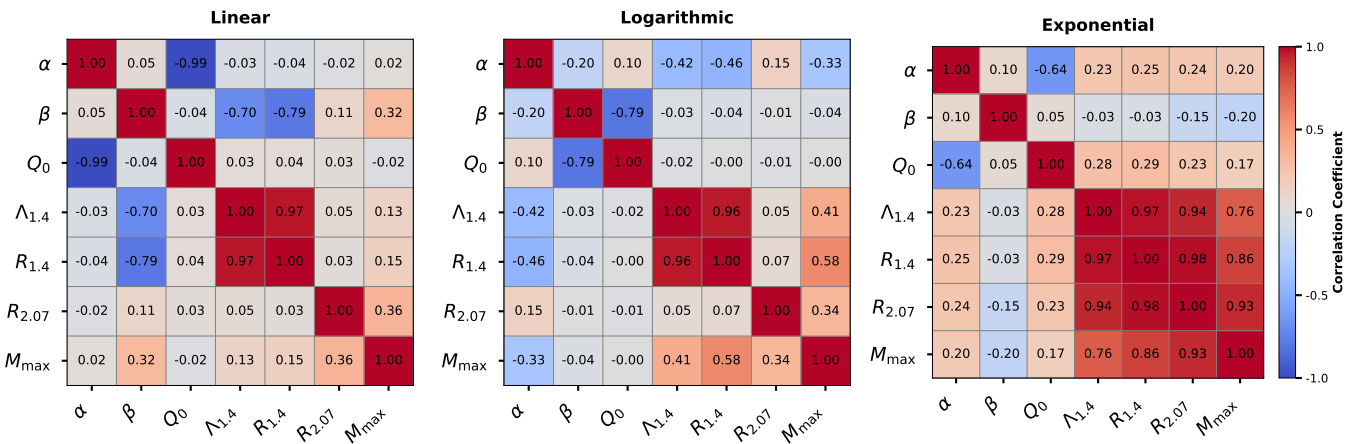


FIG. 5: The Pearson's correlation coefficients among parameters and selected NS properties for Linear (left panel), Logarithmic (Middle panel), and Exponential (right panel).

Sec. VI B. In Table IV, we listed the logarithmic values of the Bayes factor computed using Eq. (43) for all models. The interpretation of the Bayes factor is discussed in Sec. VI B 2. We consider the Exponential model as hypothesis H_2 and other models as H_1 to compute $\ln(\text{BF12})$. From the large negative values of $\ln(\text{BF12})$, it is clear that Exponential is definitely the best model in the Bayesian inference. The Bayes factors computed for all models consistently rank the models in the same order: Exponential as the best, followed by Logarithmic, then Linear.

Violin plots provide a detailed view of posterior

distributions by merging a box plot's summary statistics with a smooth density curve. This allows for easy visual comparison of features such as skewness, multimodality, and the overall spread of model parameter constraints. Figure 6 shows the Violin plots of the posterior distributions for the $f(Q)$ model parameters α (left), β (middle), and Q_0 (right) for the Linear (Lin), Logarithmic (Log), and Exponential (Exp) models. In the Exponential case, all parameter distributions are nearly Gaussian and unimodal, indicating a single, well-defined solution favored by the observed data. For the Logarithmic model, the posteriors for β and

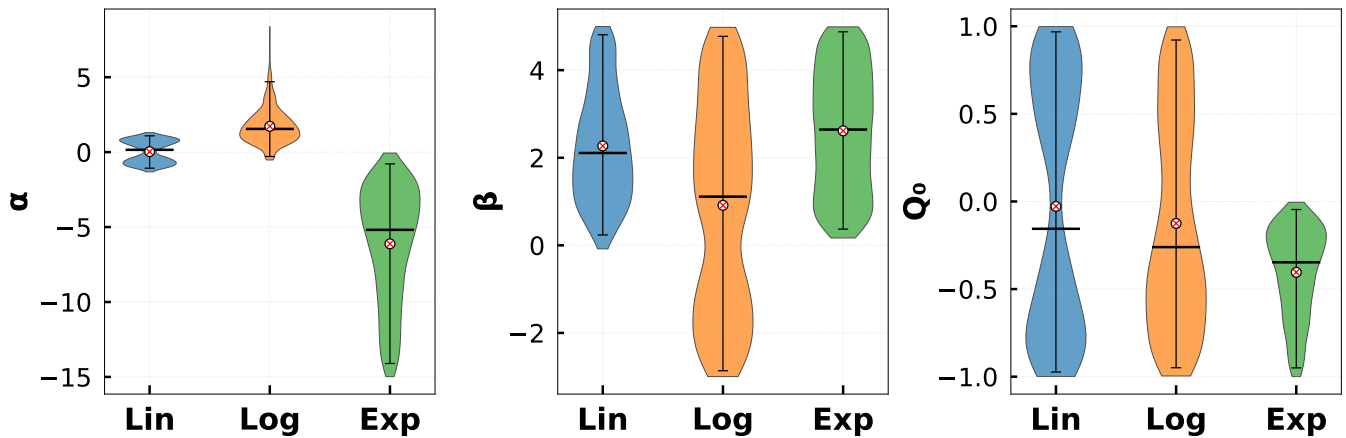


FIG. 6: Violin plots of the posterior distributions for the $f(Q)$ model parameters α (left), β (middle), and Q_0 (right) for the Linear (Lin), Logarithmic (Log), and Exponential (Exp) models.

Q_0 deviate from a perfect Gaussian shape, reflecting greater uncertainty and potential degeneracies. The Linear model shows the most pronounced issues: its α distribution is distinctly bimodal, suggesting two separate solutions, and its Q_0 posterior is very broad. This bimodality and the associated parameter degeneracies lower the model's Bayesian evidence relative to the others. This visualization highlights why the Exponential model is statistically favored, followed by the Logarithmic and then the Linear model.

VIII. SUMMARY AND OUTLOOK

We employed Bayesian inference with three modified gravity $f(Q)$ models Linear, Logarithmic and Exponential by integrating astrophysical constraints from NICER mass-radius measurements. The NICER data includes PSR J0030+0451, PSR J0740+6620, PSRJ0437+4715, and PSRJ0614+3329. For the first time in the literature on $f(Q)$ gravity, this analysis systematically confronts the theory with neutron star observables in the strong field regime.

The Exponential model appeared as the statistically preferred choice, supported by multiple lines of evidence: its Q_0 parameter is the most tightly constrained ($-0.35^{+0.20}_{-0.36}$), its posterior distributions of all parameters are nearly Gaussian and unimodal. In contrast, the Logarithmic model shows broader parameter uncertainties and mild degeneracies, particularly for β ($1.11^{+2.52}_{-3.02}$). While it predicts the highest maximum neutron-star mass ($2.36 M_{\odot}$). The Linear model exhibits pronounced bimodality in its α posterior and the broadest Q_0 distribution, reflecting strong

parameter degeneracies that reduce its statistical credibility. The tidal deformability $\Lambda_{1.4}$ and radius $R_{1.4}$ for Exponential model found to be $156.95^{+84.02}_{-41.73}$ and $11.27^{+0.53}_{-0.36}$, respectively.

Model comparisons based on the computed Bayes factors confirm this hierarchy. The logarithmic Bayes factors, $\ln(BF)$, decisively favor the Exponential model over the Logarithmic and Linear alternatives, with values of -0.35 and -1.28 , respectively. According to the established scale, this indicates strong evidence for the Exponential model. Therefore, the Exponential $f(Q)$ model emerges as the best constrained and most statistically supported description of neutron star structure among the three, highlighting its viability as a modified gravity candidate in the strong-field regime.

In the present analysis we adopted a single baseline dense-matter description (DDME2) to reduce nuclear-physics systematics and focus on the impact of the $f(Q)$ sector, with the NICER likelihood and inferred maximum mass explicitly conditioned on this choice. A natural next step is to quantify the robustness of the inferred gravity parameters against EoS uncertainties by performing Bayesian inference for alternative representative nuclear matter EoSs (RMF-based or hybrid), and performing Bayesian model comparison across EoSs in analogy with our Bayes-factor ranking of the $f(Q)$ models. More generally, one can carry out a joint (hierarchical) Bayesian inference in which the $f(Q)$ parameters and a flexible EoS parameterization (e.g., piecewise-polytropic or spectral representations) are sampled simultaneously, thereby marginalizing over the EoS and directly addressing the known degeneracy between strong-field gravity and microphysics; such joint gravity-EoS strategies have

proven informative in other modified-gravity contexts. Extending the data evidence beyond NICER (e.g., incorporating experimental nuclear data, empirical nuclear inputs, and theoretical predictions) would further help break degeneracies and tighten constraints on both sectors.

IX. ACKNOWLEDGEMENTS

S.P. acknowledges the Neutron Star Meeting 2025 held at the Institute of Mathematical Sciences (IMSc),

Chennai, India, that motivates this study. KZ acknowledge support by the CUHK-Shenzhen University development fund under grant No. UDF01003041 and UDF03003041, and Shenzhen Peacock fund under No. 2023TC0179. We also thank Dr. Tuhin Malik, Dr. Sk Md Adil Imam and Asit Karan for technical discussions.

[1] A. Einstein, *Annalen der Physik* **49**, 769 (1916).

[2] R. M. Wald, *General Relativity* (Chicago Univ. Pr., Chicago, USA, 1984).

[3] C. M. Will, *Living Reviews in Relativity* **17** (2014), 10.12942/lrr-2014-4.

[4] T. Clifton, P. G. Ferreira, A. Padilla, and C. Skordis, *Phys. Rep.* **513**, 1 (2012), arXiv:1106.2476 [astro-ph.CO].

[5] S. e. a. Perlmutter, *Astrophysical Journal* **517**, 565 (1999).

[6] A. G. e. a. Riess, *Astron. J.* **116**, 1009 (1998), arXiv:astro-ph/9805201.

[7] D. N. e. a. Spergel, *Astrophysical Journal Supplement Series* **170**, 377 (2007).

[8] M. e. a. Tegmark, *Phys. Rev. D* **71**, 103515 (2005).

[9] V. Sahni and A. A. Starobinsky, *International Journal of Modern Physics D* **9**, 373 (2000).

[10] T. Padmanabhan, *Physics Reports* **380**, 235 (2003).

[11] E. V. Linder, *General Relativity and Gravitation* **40**, 329 (2008).

[12] J. Frieman, M. Turner, and D. Huterer, *Annual Review of Astronomy and Astrophysics* **46**, 385 (2008).

[13] R. R. Caldwell and M. Kamionkowski, *Annual Review of Nuclear and Particle Science* **59**, 397 (2009).

[14] A. De Felice and S. Tsujikawa, *Living Reviews in Relativity* **13**, 3 (2010).

[15] T. P. Sotiriou and V. Faraoni, *Reviews of Modern Physics* **82**, 451 (2010).

[16] S. Capozziello and M. De Laurentis, *Physics Reports* **509**, 167 (2011).

[17] S. Nojiri and S. D. Odintsov, *Physics Reports* **505**, 59 (2011).

[18] J. Harada, *Phys. Rev. D* **101**, 024053 (2020).

[19] R. Aldrovandi and J. G. Pereira, *Teleparallel Gravity: An Introduction*, Vol. 173 (Springer, Berlin, 2013).

[20] J. W. Maluf, *Annalen der Physik* **525**, 339 (2013).

[21] J. B. Jiménez, L. Heisenberg, and T. Koivisto, *Phys. Rev. D* **98**, 044048 (2018).

[22] D. Zhao, *Eur. Phys. J. C* **82**, 303 (2022).

[23] W. Wang, H. Chen, and T. Katsuragawa, *Phys. Rev. D* **105**, 024060 (2022).

[24] J. A. Najera, C. A. Alvarado, and C. Escamilla-Rivera, *Mon. Not. Roy. Astron. Soc.* **524**, 5280 (2023).

[25] G. N. Gadbail and P. K. Sahoo, *Chin. J. Phys.* **89**, 1754 (2024).

[26] O. Sokoliuk, S. Arora, S. Praharaj, A. Baransky, and P. K. Sahoo, *Mon. Not. Roy. Astron. Soc.* **522**, 252 (2023).

[27] F. K. Anagnostopoulos, V. Gakis, E. N. Saridakis, and S. Basilakos, *Eur. Phys. J. C* **83**, 58 (2023).

[28] T. Hinderer, *Astrophys. J.* **677**, 1216 (2008).

[29] T. Hinderer, B. D. Lackey, R. N. Lang, and J. S. Read, *Phys. Rev. D* **81**, 123016 (2010).

[30] N. Andersson and K. D. Kokkotas, *Mon. Not. R. Astron. Soc.* **299**, 1059 (1998).

[31] H. Sotani, K. D. Kokkotas, and N. Stergioulas, *Mon. Not. R. Astron. Soc.* **375**, 261 (2007).

[32] J. M. Lattimer and M. Prakash, *Astrophys. J.* **550**, 426 (2001).

[33] F. Özel and P. Freire, *Annu. Rev. Astron. Astrophys.* **54**, 401 (2016).

[34] P. B. Demorest, T. Pennucci, S. M. Ransom, M. S. E. Roberts, and J. W. T. Hessels, *Nature* **467**, 1081 (2010).

[35] J. e. a. Antoniadis, *Science* **340**, 1233232 (2013).

[36] H. T. e. a. Cromartie, *Nature Astronomy* **4**, 72 (2020).

[37] E. e. a. Fonseca, *Astrophys. Jour. Lett.* **915**, L12 (2021).

[38] K. C. Gendreau and Z. Arzoumanian, *Nature Astronomy* **1**, 895 (2017).

[39] M. C. e. a. Miller, *Astrophys. Jour. Lett.* **918**, L28 (2021).

[40] T. E. e. a. Riley, *Astrophys. Jour. Lett.* **918**, L27 (2021).

[41] A. Karan, A. Kumar, M. Sinha, and R. Mallick, *Monthly Notices of the Royal Astronomical Society* **543**, 83–94 (2025).

[42] B. P. e. a. Abbott, *Phys. Rev. Lett.* **121**, 161101 (2018).

[43] E. e. a. Berti, *Class. and Quant. Grav.* **32**, 243001 (2015).

[44] S. e. a. Capozziello, *Phys. Rev. D* **93**, 023501 (2016).

[45] K. V. e. a. Staykov, *Phys. Rev. D* **90**, 023005 (2014).

[46] P. N. Moreno, A. Wojnar, and F. J. Llanes-Estrada, *Journal of Cosmology and Astroparticle Physics* **2025**, 015 (2025).

- [47] M.-K. Cheoun, C. Deliduman, C. Güngör, V. Keleş, C. Ryu, T. Kajino, and G. J. Mathews, *Journal of Cosmology and Astroparticle Physics* **2013**, 021–021 (2013).
- [48] A. V. Astashenok, S. Capozziello, and S. D. Odintsov, *Journal of Cosmology and Astroparticle Physics* **2013**, 040–040 (2013).
- [49] S. Hendi, G. Bordbar, B. E. Panah, and S. Panahiyan, *Journal of Cosmology and Astroparticle Physics* **2016**, 013–013 (2016).
- [50] S. Vilhena, S. Duarte, M. Dutra, and P. Pompeia, *Journal of Cosmology and Astroparticle Physics* **2023**, 044 (2023).
- [51] G. e. a. Raaijmakers, *Astrophys. Jour. Lett.* **918**, L29 (2021).
- [52] R. e. a. Essick, *Phys. Rev. D* **102**, 043003 (2020).
- [53] J.-L. Jiang, C. Ecker, and L. Rezzolla, *The Astrophys. Jour.* **949**, 11 (2023).
- [54] Y. Lim and J. W. Holt, *Phys. Rev. Lett.* **121**, 062701 (2018).
- [55] D. Roy, T. Malik, S. Bhattacharya, and S. Banik, *The Astrophys. Jour.* **968**, 124 (2024).
- [56] K. Nobleson, S. Banik, and T. Malik, *Phys. Rev. D* **107**, 124045 (2023), arXiv:2306.01054 [gr-qc].
- [57] B. Biswas, E. Smyrniotis, I. Liodis, and N. Stergioulas, *Phys. Rev. D* **109**, 064048 (2024).
- [58] e. a. C. J. Xia, *Commun. in Theor. Phys.* **74**, 095303 (2022).
- [59] G. A. Lalazissis, T. Niksic, D. Vretenar, and P. Ring, *Phys. Rev. C* **71**, 024312 (2005).
- [60] J. B. Jimenez, L. Heisenberg, and T. S. Koivisto, *J. Cosmol. Astropart. Phys.* **2018**, 039 (2018).
- [61] J. B. Jiménez, L. Heisenberg, and T. S. Koivisto, *Phys. Rev. D* **98**, 044019 (2018).
- [62] J. B. Jimenez, L. Heisenberg, T. Koivisto, and S. Pekar, *Phys. Rev. D* **101**, 103507 (2020).
- [63] J. F. Donoghue, *Phys. Rev. D* **50**, 3874 (1994).
- [64] W. Khyllep *et al.*, *Phys. Rev. D* **107**, 044022 (2023).
- [65] T. E. Riley *et al.*, *Astrophys. J. Lett.* **887**, L21 (2019).
- [66] M. C. Miller *et al.*, *Astrophys. J. Lett.* **887**, L24 (2019).
- [67] D. Choudhury *et al.*, *Astrophys. J. Lett.* **971**, L20 (2024).
- [68] L. Mauviard *et al.*, *Astrophys. J.* **995**, 60 (2025).
- [69] J. R. Oppenheimer and G. M. Volkoff, *Phys. Rev.* **55**, 374 (1939).
- [70] R. C. Tolman, *Phys. Rev.* **55**, 364 (1939).
- [71] R. E. Kass and A. E. Raftery, *J. Am. Stat. Assoc.* **90**, 773 (1995).
- [72] A. Jarosz and J. Wiley, *The Journal of Problem Solving* **7** (2014), 10.7771/1932-6246.1167.